

Collisions of false vacuum bubbles in cylindrical symmetry

Yu-ichi Takamizu^{1*} and David Chernoff^{2†}

¹ *Center for Computational Sciences, University of Tsukuba,
1-1-1 Tennoudai, Ibaragi 305-8577 Japan*

² *Department of Astronomy,
Cornell University, Ithaca NY 14853*

(Dated: October 1, 2018)

We explore the collision of two cylindrical bubbles in classical general relativity with a scalar field stress-energy tensor. Inside each bubble the field rests at a local minimum of the potential with non-negative energy density. Outside the field rests at zero potential, the global minimum. The calculation resolves the connection from the inner de-Sitter region to the asymptotically flat Minkowski spacetime. We choose initial conditions such that the two bubbles collide and study the full nonlinear evolution by means of a two-dimensional numerical simulation of Einstein's equations. The collision generates a strongly interacting region with spatially varying fields and potentials. These circumstances promote dynamical exploration of the potential's landscape. No horizon is present and the scalar curvature invariants eventually diverge. We speculate that Schwarzschild-like horizons will encompass only part of the complicated, interesting regions of spacetime in the analogous case of colliding spherical bubbles.

PACS numbers: 98.80.-k, 98.90.Cq

I. INTRODUCTION

The string theory landscape [1] contains numerous metastable vacua. The transition paths from one vacuum to another are of interest in the cosmological history of the universe. Inspired by this situation, we investigate the consequences of classical bubble collisions in Einstein 3+1 gravity for exploring the landscape.

We will focus on scalar field ϕ with potential $V(\phi)$ with action

$$S = \int d^4x \sqrt{-g} \left[R - \frac{1}{2} \partial_\mu \phi \partial^\mu \phi - V(\phi) \right], \quad (1.1)$$

where we set $c = G = 1$. We are interested in the situation where $V(\phi)$ has two or more local minima that permit bubble-like solutions with true and false vacua. We investigate the outcome of bubble collisions taking into account self-gravity.

The broad context is the traversal of the potential landscape from false vacuum to true vacuum and vice-versa. The general statistical formalism of transition rates [2] has been coupled with quantum field theory, including thermal fluctuations, in curved spacetime [3–5] to analyze many diverse cosmological scenarios. There are situations where the false vacuum to true vacuum transition is of central interest. The quantum mechanical transition from a de-Sitter space with positive cosmological constant at the termination of inflation in the original inflation models [6–10] is a prominent example. Here, a small region with $V_0 > 0$ tunnels, perhaps with thermal assistance, to a lower potential V_1 with $V_1 < V_0$. The de-excitation path is of natural interest in an expanding, cooling universe and the transition rate influences the probability of bubble collisions and whether the true vacuum percolates in the expanding background spacetime.

In a different cosmological context, the de-excitation rate governs how rapidly a complicated theory landscape can be scanned. A primary question in modern string theory is whether it is possible to locate a local minima of the multiverse whose potential is consistent with the small, observed value of the cosmological constant in our Universe [11].

Of course, de-excitation transitions from false to true vacua have corresponding inverse processes. Inside a bubble with small positive cosmological constant a field patch may fluctuate upward to a local minima of the potential with larger potential value. While disallowed in Minkowski space by considerations of energy conservation there

*Electronic address: takamizu@ccs.tsukuba.ac.jp

†Electronic address: chernoff@astro.cornell.edu

are suggestive general arguments that upward fluctuations will occur in de-Sitter space [12]. Fluctuations may also produce defects during de-Sitter expansion [13].

Competing microscopic forward-backward transition rates are important in the statistical description of nucleation, percolation and traversal of the landscape. The possibility of bubble collisions considerably enriches the variety of transition pathways. Collisions of true vacuum bubbles may generate short-lived pockets of false vacuum [14] that give birth to black holes. Energetic bubble collisions can mediate downward transitions and enhance the rate of exploration of vacua which are close by in field space [15]. Calculations of classical bubble collisions have been carried out for various model potentials [16–18]. The observational signatures of bubble collisions are also being explored [19–24].

In this paper we will concentrate on collisions of bubbles of false vacua. We will assume that one bubble collides with another bubble before either is hidden by an apparent horizon and before either expands beyond the cosmological horizon. We consider the simplest scalar field potential with one global minimum with $V = 0$, two distinct local minima with $V > 0$ and intervening barriers. This choice allows the study of many types of bubble collisions.

II. METRIC FOR SPHERICAL AND CYLINDRICAL BUBBLES

In 3+1 dimensional spacetime with spherical symmetry the metric with isotropic coordinates may be written $ds^2 = -\alpha^2 dt^2 + a^2(dr^2 + r^2 d\Omega^2)$ where r is a radial coordinate, $\alpha = \alpha(t, r)$, $a = a(t, r)$ and $d\Omega^2$ is the two-dimensional metric on the unit sphere (see eqn. 16 in [25]). Spherical symmetry is suitable for an isolated bubble and the evolution can be handled numerically since the relevant dynamics is 1+1 dimensional. Two spherically symmetric bubbles can collide with axial symmetry about the line of separation of their centers but the numerical solution is 2+1 dimensional and more challenging. More general collisions lead to full 3+1 dimensional problems. Instead, we will consider bubbles of a cylindrical form that vary in space perpendicular to the axis of symmetry but not along the axis. The dynamics of a single bubble is 1+1 dimensional and the collision of two bubbles with aligned axes is 2+1 dimensional. We adopt this simplified geometry as a first step in the study the interactions of bubbles.

The metric for a single cylindrically symmetric bubble has the form

$$ds^2 = e^{2A} \left(-dt^2 + dr^2 + r^2 \tilde{\beta}^2 d\theta^2 \right) + e^{2(B-A)} dz^2, \quad (2.1)$$

where the three metric functions A , B and $\tilde{\beta}$ depend upon t and r (the two dimensional cylindrical radius). This form is equivalent to the general expression given by Thorne (eqn. 2 in [26]). We use θ as the polar angle since we will retain the symbol ϕ for the scalar field potential. All functions depend upon t and r but not θ . This metric has axial symmetry about the z-axis and translational symmetry along the z-axis and we refer to it as a “cylinder system”.

The deficit angle for the cylinder system is δ , where $\tilde{\beta} = (2\pi - \delta)/2\pi$. The simplest example of the deficit angle occurs in an ideal one-dimensional cosmic string with tension μ . Solving Einstein’s equations gives $\delta = 8\pi\mu$ constant everywhere and ill-defined at $r = 0$. In general, the deficit angle is related to the mass-energy distribution within the cylinder system and varies with r . We will work in the limit that δ is initially small and remains small. The dynamical equations for $\tilde{\beta}$ are of the form

$$\tilde{\beta}_{tt} = \tilde{\beta} \times \mathcal{C} - B_r \tilde{\beta}_r + B_t \tilde{\beta}_t, \quad (2.2)$$

where \mathcal{C} is schematic for the left-hand side of the constraint eq. 3.7 below. When the constraint equation is satisfied $\mathcal{C} = 0$. So, if $\tilde{\beta}_r = \tilde{\beta}_t = 0$ initially and if the constraint equation is exactly imposed then $\tilde{\beta} = 1$ and $\delta = 0$. Henceforth, we drop the spacetime dependence for $\tilde{\beta}$, fixing $\tilde{\beta} = 1$.

Now the form of the metric for the cylinder system becomes

$$ds^2 = e^{2A} \left(-dt^2 + dx^2 + dy^2 \right) + e^{2(B-A)} dz^2, \quad (2.3)$$

$$A = A(r, t), \quad B = B(r, t), \quad (2.4)$$

where $dr^2 + r^2 d\theta^2 = dx^2 + dy^2$. For a single bubble the maximally symmetric metric form has $B = 2A$. Numerical calculations show that an initial state of maximal symmetry evolves in such a way that the symmetry is broken but that the deviation is small. Later, we will find that this remains true even for two interacting bubbles.

Up to now we have considered a single cylinder system with axial symmetry. For two bubbles the axial symmetry is broken. Assume the bubble deficit angle is small, the metric approaches Minkowski and the scalar field is uniform far from the cylinder. For two distant, parallel cylinders of this sort at rest with respect to each other we promote the two separate A functions (one for each cylinder) to a single function A for all spacetime. Likewise for B . The promoted A and B will depend upon r , θ and t , or equivalently, x , y and t . For close, interacting cylinders (either because the outer

geometry is not Minkowski or because the scalar field varies) our working ansatz is to replace the occurrences of $A(r, t)$ and $B(r, t)$ in the cylinder system with the promoted $A(x, y, t)$ and $B(x, y, t)$, respectively, while holding the form of the metric fixed. We continue to assume $\delta = 0$ in the interacting system. This ansatz yields three evolution equations and five constraint equations that extend the original three evolution equations and three constraints of the cylinder system. The hierarchical relationship of extended to original systems is straightforward: when $A(x, y, t) \rightarrow A(r, t)$, $B(x, y, t) \rightarrow B(r, t)$ and $\phi(x, y, t) \rightarrow \phi(r, t)$ the evolution equations for $A_{tt}(x, y, t)$, $B_{tt}(x, y, t)$ and $\phi_{tt}(x, y, t)$ reduce to the equivalent expressions for $A_{tt}(r, t)$, $B_{tt}(r, t)$ and $\phi_{tt}(r, t)$, respectively. Likewise, the five constraints reduce to the three independent constraints of the cylinder system.

Typically, the initial conditions we choose have maximal symmetry but the system can/will evolve away from maximal symmetry, i.e. $B = 2A$ is not imposed. We generalize the scalar field $\phi(r, t)$ to $\phi(x, y, t)$.

III. POTENTIAL

We will consider a potential that allows for two bubble vacua at $\phi = \phi_1$ and ϕ_2 with $V(\phi_1) > 0$ and $V(\phi_2) > 0$. These will collide in a background region with $\phi = \phi_0$ with $V(\phi_0) = 0$. The specific form is

$$V(\phi) = b_0 \left(\frac{1}{12}(\phi^4 - 1)^2 - (\phi^2 - 1)^2 + \frac{1}{8}(\phi - 1) + c_0 \right). \quad (3.1)$$

The global minimum of the potential occurs at $\phi = \phi_0 = -0.031$ and the constant c_0 sets $V(\phi_0) = 0$. The shape of the potential is shown in Fig. 1. The two local minima ϕ_1 and ϕ_2 have the following properties:

$$V(\phi_1) < V(\phi_2), \quad \phi_1 = -1.42, \quad \phi_2 = 1.40. \quad (3.2)$$

The cosmological constant for each bubble is $\Lambda_{1,2} = V(\phi_{1,2})$. The multiplicative factor b_0 sets the scale of the potential.

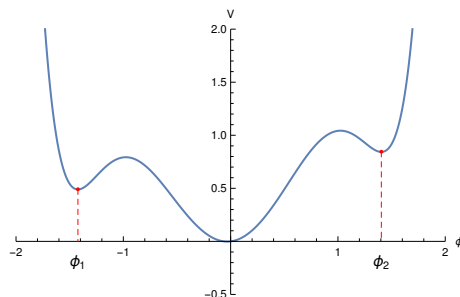


FIG. 1: The scalar field potential $V(\phi)$, shown for $b_0 = 1$, possesses 2 local minima with positive cosmological constant and 1 global minimum with zero cosmological constant. The transition of field from the global minimum (Minkowski spacetime) to one of the local minima (de-Sitter spacetime) by way of the local maximum forms the bubble wall.

In the limit of uniform, time-independent ϕ the conformal Hubble constants (the physical time is $\tau = \int e^A dt$; the conformal time is t) are

$$H_{1,2} \equiv \partial_t A_{1,2} = e^{A_{1,2}} \sqrt{\frac{V(\phi_{1,2})}{3}} \quad (3.3)$$

for bubbles 1 and 2. The rate of expansion is proportional to $\sqrt{b_0}$.

The Einstein equations and the scalar field equation of motion yield the dynamical equations

$$4A_{tt}(t, x, y) = -2A_t^2 + 4(A_{xx} + A_{yy}) + 2(A_x^2 + A_y^2) - (\phi_t^2 - \phi_x^2 - \phi_y^2) + 2e^{2A}V(\phi), \quad (3.4)$$

$$2B_{tt}(t, x, y) = B_{xx} + B_{yy} - (A_x^2 + A_y^2) + 2(A_x B_x + A_y B_y) + (A_x - B_x)^2 + (A_y - B_y)^2 - 2(A_t - B_t)^2 - \phi_t^2 + 2e^{2A}V(\phi), \quad (3.5)$$

$$\phi_{tt}(t, x, y) = -B_t \phi_t + \phi_{xx} + \phi_{yy} + B_x \phi_x + B_y \phi_y - e^{2A} \partial_\phi V(\phi), \quad (3.6)$$

plus constraint equations

$$B_{xx} - B_{yy} + A_x^2 - A_y^2 + 2A_y B_y - 2A_x B_x + (A_x - B_x)^2 - (A_y - B_y)^2 + \phi_x^2 - \phi_y^2 = 0, \quad (3.7)$$

$$2A_t(2B_t - A_t) = 2(B_{xx} + B_{yy}) + 2(A_x - B_x)^2 + 2(A_y - B_y)^2 + \phi_t^2 + \phi_x^2 + \phi_y^2 + 2e^{2A}V(\phi), \quad (3.8)$$

$$B_x(2A_t - B_t) + 2A_x(B_t - A_t) - B_{xt} = \phi_x \phi_t, \quad B_y(2A_t - B_t) + 2A_y(B_t - A_t) - B_{yt} = \phi_y \phi_t, \quad (3.9)$$

$$B_y(2A_x - B_x) + 2A_y(B_x - A_x) - B_{xy} = \phi_x \phi_y, \quad (3.10)$$

where A_t , A_x and A_y denotes partial derivatives of A with respect to t , x and y , respectively. The constraint equations are solved for the initial conditions and, once satisfied, are automatically preserved by evolution. We refer to equation (3.8) as the FLRW equation for the whole spacetime including two bubbles.

IV. NON-INTERACTING BUBBLE SOLUTIONS

First we will consider two thin-walled bubbles with stationary centers that lie far apart. We work in a two-dimensional box with coordinates $x = [-20, 20]$ and $y = [-20, 20]$ and take the centers of two bubbles to be $(x_1, y_1) = (-7, 0)$ and $(x_2, y_2) = (7, 0)$. The initial bubble radii are $R_{1,2} = 4$ where the bubble rim in (x, y) space satisfies

$$R_{1,2} = \sqrt{(x - x_{1,2})^2 + y^2}. \quad (4.1)$$

We will specify the initial metric and scalar field configuration by using the above equations. For the metric, we fix $B = 2A$ at the initial time (maximal symmetric case). Eqns. (3.4) and (3.5) yield spatial differential equations without any time derivative terms. Holding $\phi_t = \phi_{tt} = 0$ and using (3.6) gives

$$2(A_{xx} + A_{yy}) - 2(A_x^2 + A_y^2) + \phi_x^2 + \phi_y^2 = 0, \quad (4.2)$$

$$\phi_{xx} + \phi_{yy} + 2A_x\phi_x + 2A_y\phi_y - e^{2A}\partial_\phi V(\phi) = 0. \quad (4.3)$$

An isolated bubble has zero field gradient at the bubble center and the field approaches zero at infinity. We approximate by setting $\phi = \phi_i$ and $A = A_i$ within bubble i ($i = 1$ and 2) and $\phi = A = 0$ on the computational box boundaries. Numerically, we choose $A_1 = 0.25$ and $A_2 = 0.3$. Once $A > \mathcal{O}(1)$ large changes in the metric will occur on account of the appearance of the factor e^{2A} .

The numerical solution is based on approximating the functions $A(t, x, y)$, $B(t, x, y)$ and $\phi(t, x, y)$ at a given time by function values on a grid with points separated by $\Delta x = \Delta y = 0.01$ of total size 4001×4001 . At $t = 0$ the nonlinear constraint equations are converted to finite difference form and solved using Newton-Raphson techniques while holding the region within the rim and along the computational boundaries fixed. Satisfying equations (4.2) and (4.3) in cylinder symmetry in the (x, y) plane automatically satisfies the individual equations in (3.7) and (3.10). The initial spatial solutions for metric and scalar field of two bubbles (different vacua) are illustrated in Fig. 2.

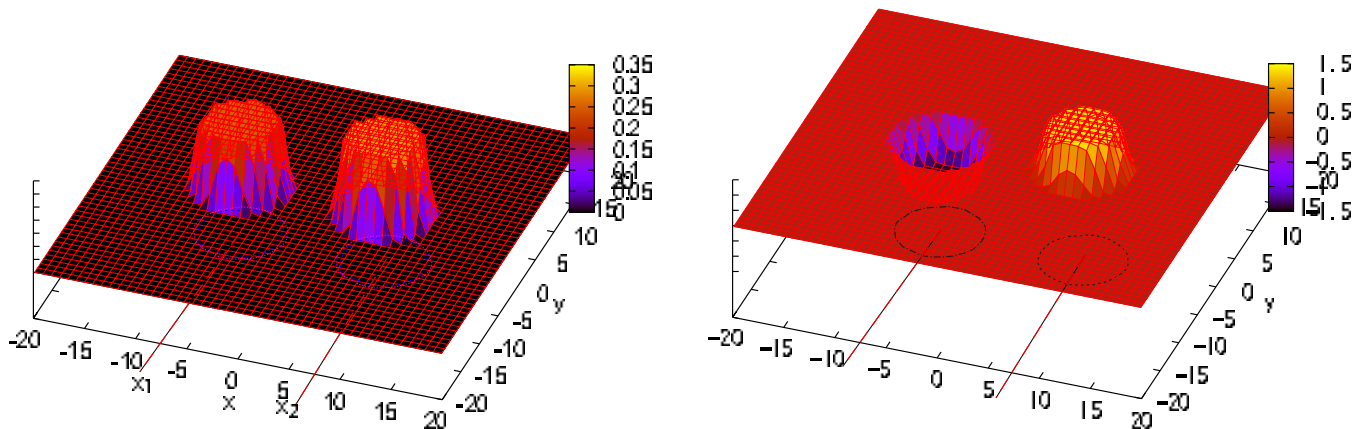


FIG. 2: Snapshot of metric coefficient $A(x, y, t)$ (left) and field $\phi(x, y, t)$ (right) in the x - y plane perpendicular to the axis of symmetry at initial time $t = 0$. The surface plots of A and ϕ are also color coded by value. The red dashed lines below the surface mark the x coordinate of the center of the bubble. The circular lines below the surface trace the bubble rims.

Once we have found the initial spatial solutions $A(t = 0, x, y)$ and $\phi(t = 0, x, y)$, we infer the initial time derivatives $A_t(t = 0, x, y)$ and $\phi_t(t = 0, x, y)$ by solving the other constraint equations (3.8) and (3.9). There are effectively two equations for two variables A_t and ϕ_t since the second equation of (3.9) is same as the first one due to symmetry of the isolated bubble. At the box edge, far outside the bubble, we impose $A_t = \phi_t = 0$ (flat Minkowski space, stationary field at the global minimum) and inside the bubble we impose $\phi_t = 0$ (stationary field with the vacuum expectation value). We infer the Hubble expansion of the bubble (3.3) from the FLRW equation (3.8). The transition near the bubble wall has non-trivial initial time derivatives in the metric and field that follow from the above choices. We do not impose these quantities.

With the initial values (A , $B = 2A$ and ϕ) and time derivatives (A_t and ϕ_t) we solve the dynamical equations (3.4), (3.5) and (3.6) for time evolution (see Fig. 3). The internal metric grows in a manner consistent with the choice of the local cosmological constant. Within the bubbles, $A_{1,2}(t) \simeq H_{1,2}t + A_{1,2}|_{t=0}$ at early times $t < \mathcal{O}(1)$. Later, $A_{1,2}$ grows more rapidly. We find that the metric coefficient B approximately tracks A in the sense $B \sim 2A$ (not illustrated

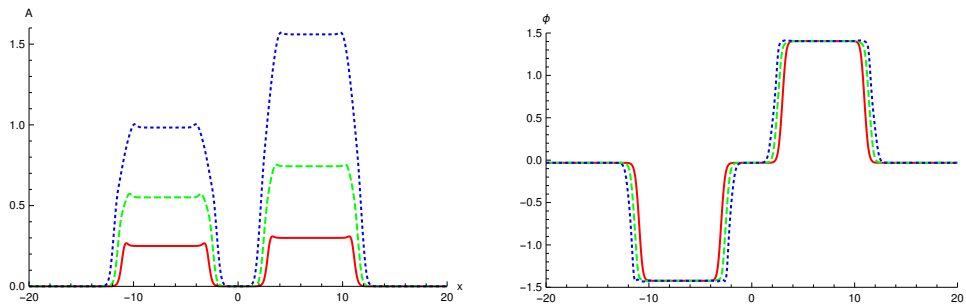


FIG. 3: The figure shows the evolution of the metric function A (left) and scalar field ϕ (right) for spacetime with two initially isolated bubbles. The bubble at $x < 0$ has field $\phi = \phi_1$, the one at $x > 0$ has $\phi = \phi_2$. The bubbles are surrounded by Minkowski spacetime with $\phi = \phi_0$. The bubble rims are symmetric in y about $y = 0$. The left panel gives three successive one-dimensional cuts of the metric function, $A(t, x, y = 0)$ for $t = 0$ (red), 0.5 (green) and 1 (blue). The bubble interiors experience de-Sitter-like expansion. Since $V(\phi_2) > V(\phi_1)$ the growth of A on the right is larger than on the left. The background spacetime has constant A . The right panel shows $\phi(t, x, y = 0)$ along the same one-dimensional cut and at the same set of times. The field transition from one minimum to another is numerically well-resolved in the calculations. Over the short time interval plotted, each wall expands outward at approximately constant, relativistic speed. The two bubbles will eventually interact. These calculations use $b_0 = 1$.

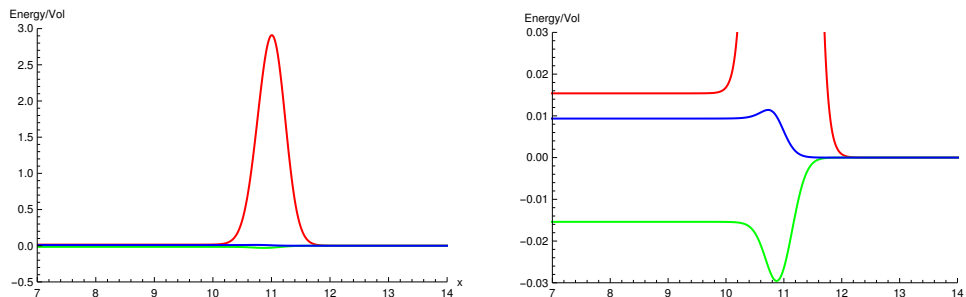


FIG. 4: The figure shows the energy density ρ (red), the pressure P (green) and the metric contribution A_t^2 (blue) for the bubble near the beginning of the simulation. The left hand figure shows the full range of variation. The right hand figure shows an expanded view of the smaller contributions near the shell.

in the figure). More precisely, $B < 2A$ at later time and the difference $|B - 2A| < 10^{-2}$ is small. Maximal symmetry breaks and manifests as the shrinkage of the ratio of the length in z -direction to that in the x - y directions. The ratio is $\propto e^{2(B-2A)}$.

Fig. 3 also shows that each bubble expands on account of the choice of initial conditions. The plots show an advancing time sequence of profiles of the metric function A and the scalar field ϕ before the individual bubbles begin to interact. The right hand plot shows that the rim of the bubble expands with coordinate speed $\dot{R} \sim 0.8 - 0.9$ (where the speed of light is 1). The field transition from inside to outside the bubble is well-resolved by the numerical grid. Its detailed shape is determined by the form of the scalar potential that connects the two minima.

Three physical effects control the evolution: the energy density inside the bubble (that of the false vacuum) and the surface tension of the bubble (as the scalar field surmounts the barrier between false and true vacua) are attractive. These pull the wall toward the center of symmetry. Within the bubble the negative pressure dominates the FLRW equation and drives the interior's exponential expansion. Finally, the jump in pressure at the wall (from inside to out) creates an additional inward directed force on the wall. Fig. 4 shows the local density $\rho = (1/2)(\phi_t^2 + \phi_x^2 + \phi_y^2) + e^{2A}V$, pressure $P = (1/2)(\phi_t^2 - \phi_x^2 - \phi_y^2) - e^{2A}V$ and metric contribution $A_t(2B_t - A_t)/3 \simeq A_t^2$ as they appear in the FLRW equation. The left hand plot shows the dominance of the energy density within the transition region of the shell. By comparison, the interior pressure is small but dominant within the interior. The right hand plot shows that ρ , P and A_t^2 are comparable within the false vacuum bubble. Based on the scale of the contributions we expect the shell to collapse even while the interior inflates.

Many investigations have characterized the general relativistic dynamics of models possessing a thin shell with surface tension that separates a spherical false vacuum interior from an asymptotically flat exterior. [27–32]. Suzuki et al [33] provide a solution for a thin cylindrical bubble with false vacuum interior and flat exterior. Their coordinates

differ from ours. In their description the rim motion is equivalent to particle motion in a potential. They found the simple result that the bubble wall which begins at small radius cannot reach infinity but must fall back to the origin.

To compare our solution quantitatively with theirs we transformed our initial coordinates for the bubble rim with respect to the bubble center ($\Delta r = 6$ and coordinate velocity, $\dot{r} = dr/dt = 1$) to their system of coordinates, solved for the rim motion and transformed the result back to our own system.¹ The plot shows the Suzuki solution for the bubble rim and the rim position inferred from the maximum total energy density in our coordinate system. In both systems the false vacuum bubble collapses.

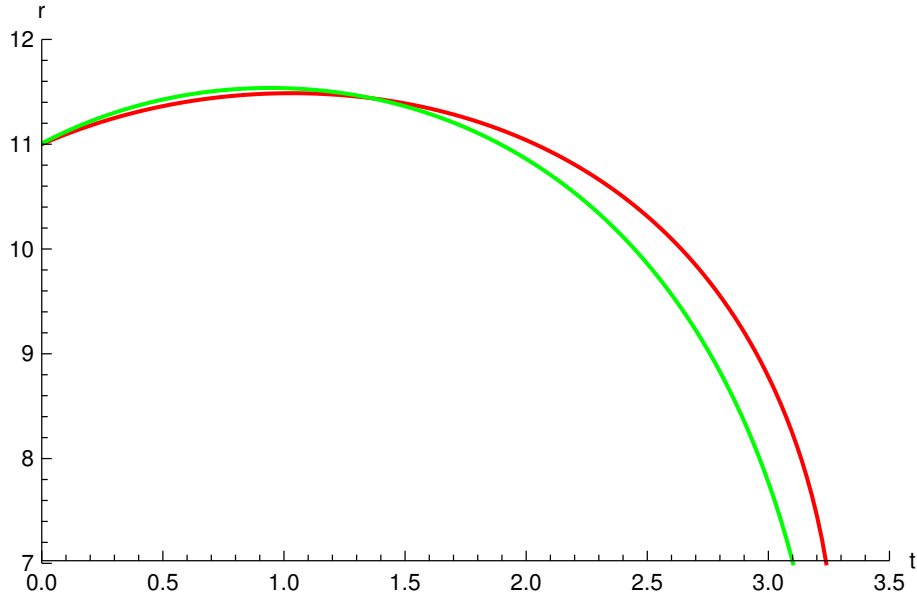


FIG. 5: A comparison of the shell position based on Suzuki's thin shell solution (red) and a numerically calculated (green) bubble like those on the right side of fig. 3. The bubble center is at $x = 7$ and the initial radius is 4. The rim position in the numerical simulation is based on the maximum total energy density.

In our coordinates the positive, nearly constant potential within the bubble implies fixed Hubble value within. Physical separation grows in an exponential fashion. As discussed by [30, 31, 34] for spherical bubbles, an observer in the false vacuum expects to see inflation whereas one near the transition between false and true vacuum (assumed thin) expects to see that inward directed forces govern the wall motion. In our case, the thickness of the wall becomes important. A gradient in the Hubble constant (rate of inflation) inevitably appears. In our computational coordinates, the inner part of the wall traces the thin shell's motion. It surrounds the nearly flat, false vacuum interior and collapses in the manner described by the Suzuki solution. The interior region is inflating at the maximum rate. The outer parts of the wall move outward with coordinate velocities close to 1 and inflate at smaller rates. The transition shears the wall into a new, bridge-like region with varying Hubble expansion. This phenomena also implies that the two neighboring bubbles in fig. 3 will begin to interact even though the rims would not meet in the thin wall treatment.

Fig. 6 plots the Kretschmann scalar curvature ($K = R^{abcd}R_{abcd}$) at three successive moments of time for the bubble on the right. The metric, scalar field and energy density are shown in Fig. 7. In a de-Sitter space with Hubble constant H the Kretschmann scalar $K = 24H^4$. This is equivalent to $K = (24/9)e^{4A}V^2$ for homogeneous potential V . Now V varies by $< 30\%$ from inside the bubble (false vacuum is $V(\phi_2)$) to the local maximum of the potential (near $\phi \sim 1$; see Fig. 1). So, it is noteworthy that K in the regions where A is maximum (inner parts of the bubble) is subdominant to K near the rim. The quadratic invariant is large near the transition *just outside* the thin shell rim. It's divergence is likely the signature of the inner false vacuum stretching or detaching from the outer Minkowski

¹ Suzuki's coordinates are ρ and T . Here, ρ is measured about the line of symmetry. Ours are Δr and t where Δr is r measured about the bubble center. The relationship is $\rho = \int e^A dr$ and $T = \int e^A dt$ where $A = A(t)$ has been taken to be only a function of time inside the bubble. We inferred the surface tension for our potential by direct numerical integration of the false to true vacuum transition from interior to exterior $\sigma = \int \rho dr$ where $\rho = \frac{1}{2}\dot{\phi}^2 + e^{2A}V(\phi)$. This gives $G\sigma = 1.32$. The corresponding terms for pressure and metric yield -2.8×10^{-2} and 6.4×10^{-3} respectively. We solved for the motion $\rho(T)$ using their eqns. 3.7a-c and then transformed the results back to $\Delta r(t)$ in our own system.

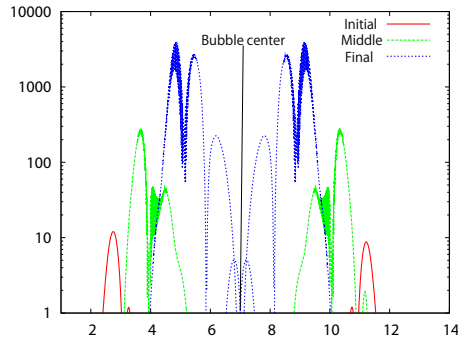


FIG. 6: The Kretschmann scalar as a function of position at three times $t = 0, 2.4$ and 2.7 during the simulation, labeled initial, middle and final respectively in the plot. The diverging curvature tracks the rim position of the Suzuki solution.

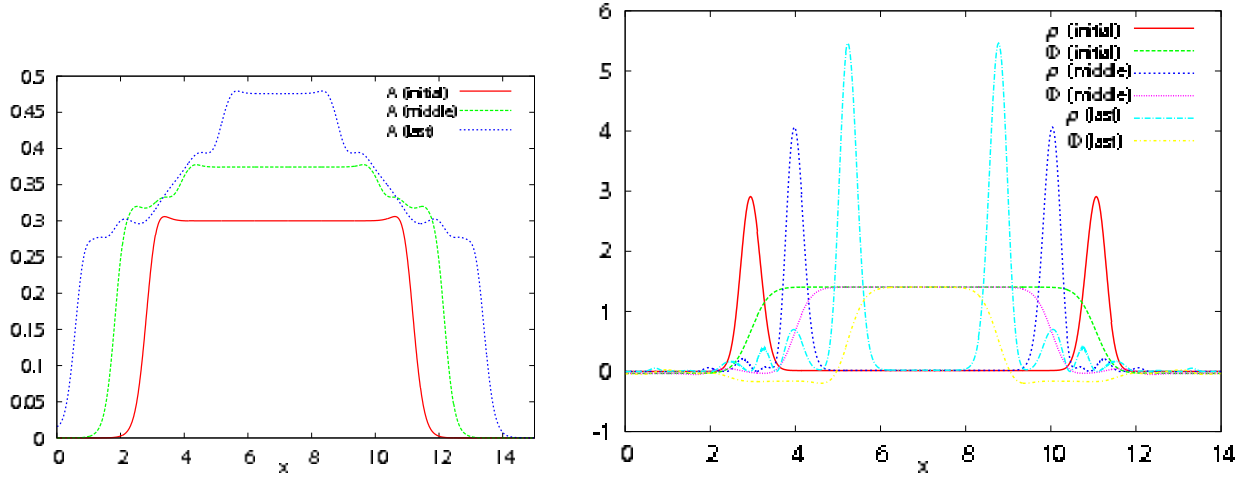


FIG. 7: The time evolution of the metric A , scalar field ϕ and energy density ρ for one contracting single bubble. The initial, middle and final labels refer to the same times as in Fig. 6. The left panel shows that the metric increases inside while the wall region which separates the inside from outside diffuses in both directions. The right panel shows the peak of the energy density and the point of the scalar field transition move inward with time. The maximum energy density tracks the thin rim location in the Suzuki model.

space. The scalar exponentially increases within a few time steps of size $\Delta t = 2.5 \times 10^{-4}$ and we halt the calculation at that point.

V. NUMERICAL ACCURACY OF SOLUTIONS

We describe three different checks on the accuracy of the runs: (i) comparison of 1+1 and 2+1 results for a single bubble, (ii) the fidelity of the initial transition profile, and (iii) constraint violations.

A. Numerical accuracy

As a check on numerical accuracy, we compared the evolution of a single isolated bubble calculated using two dimensional Cartesian coordinates to one calculated with one dimensional polar coordinates. Fig. 8 shows the result of A and B for a single isolated bubble's evolution using the 2+1 $((x, y, t))$ and 1+1 $((r, t))$ systems. The answers should be identical so the observed differences are indicative of the size of numerical error. The 1+1 system has 2000 radial zones while the 2+1 system has 10^6 zones. The 1+1 system has effectively 5 times more points per given area than the 2+1 system so we anticipate the 1+1 results are more accurate.² The results are approximately the same with the biggest notable difference to be found in the quantity $B - 2A$ at the bubble rim. Recall that the ratio of the length in the z -direction to that in the r -direction is $e^{2(B-2A)}$ which is > 1 in the 1+1 case but < 1 in the 2+1 case. These differences are indicative of the intrinsic errors in the evaluation of the metric coefficients. Fig. 9 compares

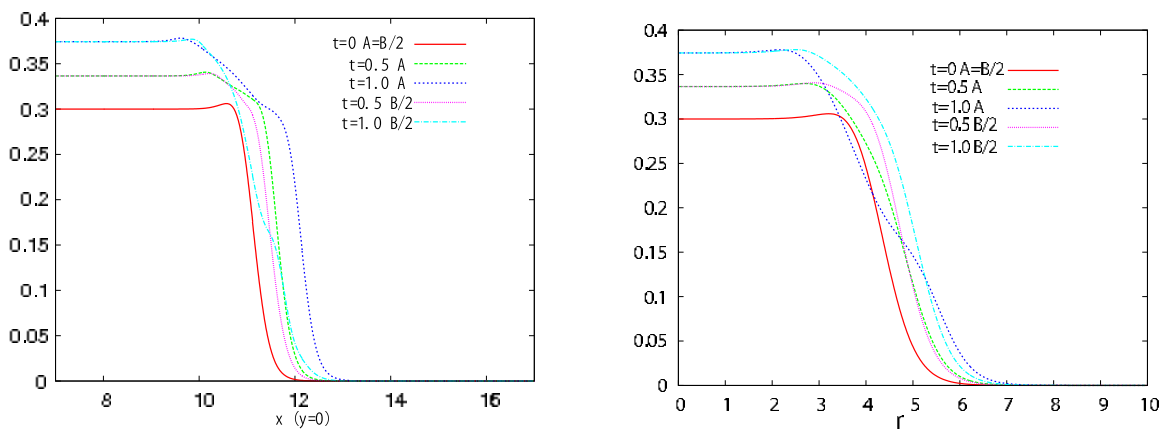


FIG. 8: The metric functions A and B are compared for one isolated bubble's evolution (snapshots at $t = 0, 0.5$ and 1) calculated in two different coordinate systems. The answers should be identical so the differences are an indication of the intrinsic numerical errors. On the left the 2+1 Cartesian system (x, y, t) with bubble center at $(x, y) = (7, 0)$ is used; on the right the 1+1 cylinder system (r, t) with $r = \sqrt{(x-7)^2 + y^2}$ and bubble center at $r = 0$ is used. The initial conditions are identical. We expect the 1+1 results to be more accurate based on the density of the grid and we infer that the differences reflect the characteristic size of the errors in the 2+1 treatment.

the field ϕ for the 2+1 and 1+1 simulations. The 2+1 simulation apparently has a steeper transition than the 1+1 simulation. The 2+1 calculation also appears to have some oscillations in inner bubble edge that are not present in the 1+1 case. The bubble shears in both treatments. The inner region tracks the thin wall limit and outer region moves outward in coordinates position, with half-maximum ϕ at nearly the same point.

B. Initial bubble profile

The Hubble constants are $H_1 = \sqrt{b_0}0.520$ and $H_2 = \sqrt{b_0}0.716$. In fig. 10, we change $b_0 = 1$ to $b_0 = 0.01$ and observe, as expected, that the Hubble expansion is about 1/10-th of the previous case. We will typically use $b_0 < 1$ to limit the extent of exponential growth during the collisions we study. With the smaller b_0 an profile change becomes apparent, the bubble transition develops a horn-like structure near the rim as the field relaxes. This is related to the

² For the 1+1 system we repeated the calculations with 1000, 1500 and 2000 points and observed effectively identical results for the latter two cases.

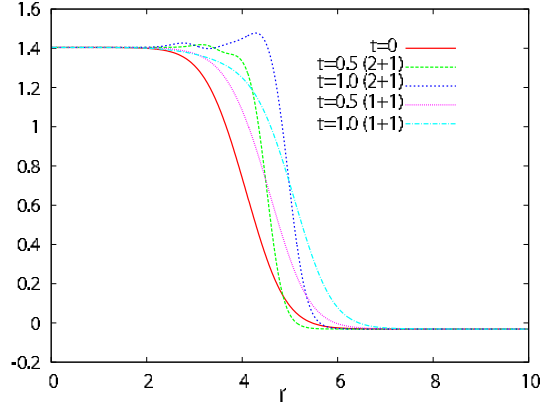


FIG. 9: Same as Fig. 8 except for $\phi(x, y, t)$ and $\phi(r, t)$ at selected times.

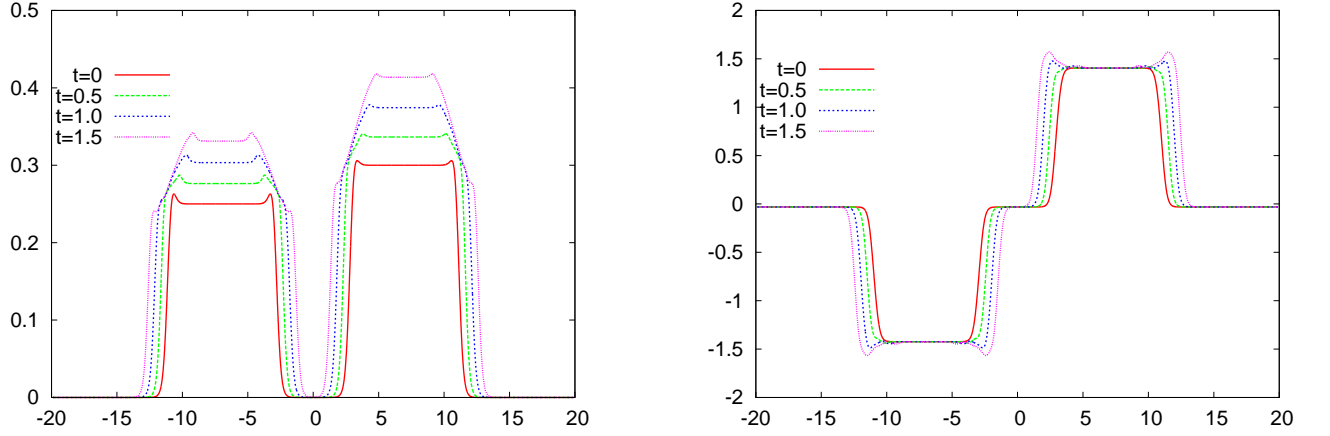


FIG. 10: The metric function A and scalar field ϕ for spacetime with two evolving, isolated bubbles. Same as Fig. 3 but with $b_0 = 0.01$.

fact that the initial bubble profile is approximate as described above: we start with the field ϕ held fixed throughout the finite volume of the bubble and at the edges of the box. It would be more realistic to impose zero radial field derivative at the bubble center and let the field vary everywhere between the center and the edges of the box. That is essentially what happens once the simulation begins: the field profile relaxes as it climbs the barrier separating the two minima. As the potential energy decreases the field kinetic and gradient energy contributions become relatively larger and their effect at the rim is more pronounced.

C. Constraints

We have also checked the development of constraint violations which is closely related to the accuracy with which we can solve the equations of motion as well as our small deficit angle approximation. For the effectively isolated bubble simulations (illustrated in figs. 2, 3, 4, 5, 6, 7) we find eqn. 3.7 is satisfied to a relative error of $< 10^{-3}$ (the residual result for eq. 3.7 divided by the sum of the absolute value of each separate term) until the Kretschmann scalar diverges near $t = 3$. The relative error is illustrated at 5 snapshots in fig. 11. The constraint violation is not monotonically increasing although it does tend to grow with time.

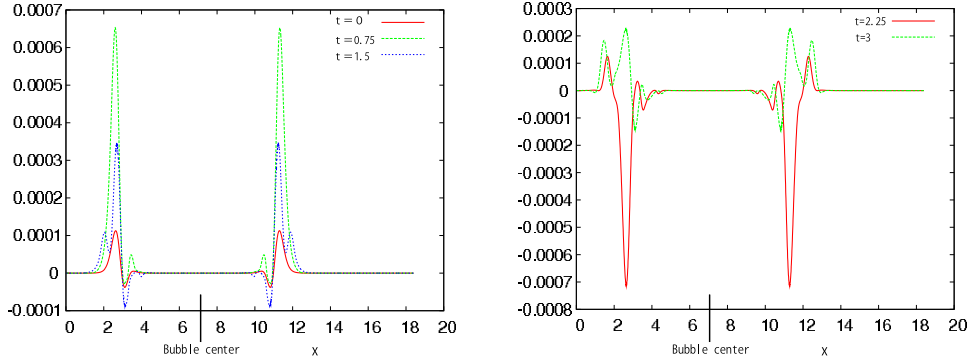


FIG. 11: The constraint violation in eqn. 3.7 at three early (left) and two later (right) times.

VI. INITIAL CONDITIONS FOR MOVING BUBBLES

We outline our general method to construct initial data for an arbitrary collision between two moving, hitherto non-interacting, bubbles. We can transform an isolated bubble solution from frame S to another frame S' when one frame moves with constant velocity with respect to the other. This is a simple Lorentz transformation. In our problem S is the frame in which a bubble has nucleated (bubble center is at rest) and S' is the collision frame. In our setup with two bubbles the left and right bubbles do not interact initially because they are separated by Minkowski space ($A = B = \phi = 0$) and the rims expand at less than the speed of light. We boost each bubble separately and stitch two halves at $x' = 0$ together to create initial conditions that will eventually give rise to a collision.

Let the origin of S move with velocity W' in S' . We want the bubble at position $x = x_1 < 0$ to move towards the origin in S' ; we take $W' > 0$ and write the desired motion for bubble 1 as $W' = W'_1 = v$. Likewise for the bubble at position $x = x_2 > 0$ we want $W' < 0$. Here, we write $W' = W'_2 = -v$. The Lorentz transformations are

$$t = \gamma(t' - W'x'), \quad x = \gamma(x' - W't'), \quad z = z', \quad (6.1)$$

for velocity $W' = \pm v$ and $\gamma = 1/\sqrt{1-v^2}$. We need not adopt $W'_1 = -W'_2$ as long as the transformed bubbles remain well-separated at $t' = 0$. Note that at time $t' = 0$ we have $t = -\gamma W'x' = -xW' > 0$ because $x_1 < 0$ has $W'_1 > 0$ and $x_2 > 0$ has $W'_2 < 0$. The initial condition slice at $t' = 0$ is shown in Fig. 12.

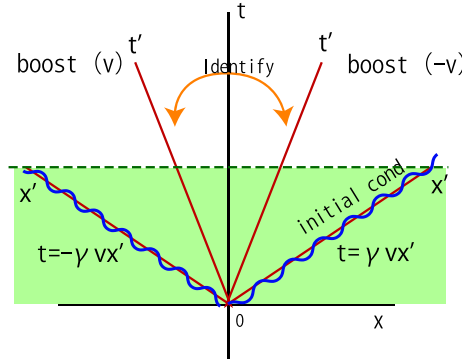


FIG. 12: A schematic picture in frame S illustrating times of simultaneity for two different boosted frames S' . To the right of the origin the boost is $-v < 0$; to the left it is $v > 0$. We solve the dynamical equation for A , B and ϕ for isolated bubbles in frame S throughout the spacetime region shaded green. We boost these solutions to frame S' (separately on the right and left sides) and infer initial conditions in the collision frame.

The form of the metric (2.4) is invariant under this transformation. The new scalar function A' is A evaluated at the transformed coordinates, i.e. $A'(t', x', y') = A(t, x, y)$ where t , x and y are understood to be functions of t' , x' and y' according to the Lorentz transformation with the appropriate boost $W' = \pm v$. Omitting the independent variables

we have schematically

$$A'|_{t'=0} = A|_{t=-\gamma W'x'} , \quad (6.2)$$

$$A'_{t'}|_{t'=0} = \gamma A_t|_{t=-\gamma W'x'} - \gamma W' A_x|_{t=-\gamma W'x'} . \quad (6.3)$$

The initial data is derived from two slices of evolved bubble solutions in the original coordinate system where $t = -xW' > 0$ as illustrated in Fig. 12. We infer ϕ' and $\phi'_{t'}$ at $t' = 0$ in an identical fashion.

Once we have found the metric and the scalar field (values and time derivatives), we integrate equations (3.4) and (3.6) in the new coordinates. Henceforth, we drop the explicit use of primes and simply refer to the coordinates in the collision frame as t , x and y .

We advance the solution with small time steps $\Delta t = 10^{-4}$ using an explicit, 4th-order Runge-Kutta method to update A , B and ϕ . The spatial derivatives are formed by finite difference approximations. Fig. 13 shows the evolution of one bubble in the collision frame. The plot on the right shows that the wall moves at nearly the speed

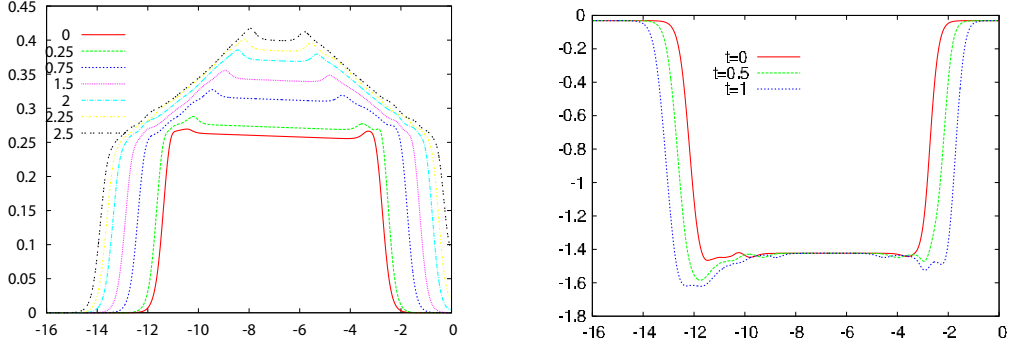


FIG. 13: We plot one boosted bubble solution in the collision frame along $y = 0$ at three times $t = 0$ (red), $t = 0.5$ (green) and $t = 1$ (blue). A (ϕ) is shown in left (right) figure. The boost is $v = 0.1$ in this region. In the left figure the highest point of A lies close to the inner edge of the false vacuum. It moves upward and rightward with time, tracking the motion of the thin shell. In the accompanying right hand figure we see the motion of the outer, transition regions. Both walls expand (time snapshots from red to blue) at close to $v = \mathcal{O}(1)$, much larger than that of the boost itself.

of light to the left at small x . In the collision frame the bubble rim moves with velocity

$$\dot{R}_{coll} = \frac{dx}{dt} + \frac{\dot{R}_{nuc}}{1 + \frac{dx}{dt} \dot{R}_{nuc}} , \quad (6.4)$$

where the boost velocity $\frac{dx}{dt} = \pm v$ and \dot{R}_{nuc} is the rim velocity in nucleation frame. With $\frac{dx}{dt} = 0.1$ and $\dot{R}_{nuc} = 0.9$ the total velocity $\dot{R}_{coll} = 0.92$. In this numerical example the total velocity of approach is dominated by the bubble expansion.

VII. BUBBLES COLLIDE AND BEGIN TO INTERACT

Fig. 14 shows the collision of two bubbles. The left hand bubble is the bubble whose isolated evolution was described in the previous section. The figure shows the metric function A and the field ϕ along a slice through the bubble centers.

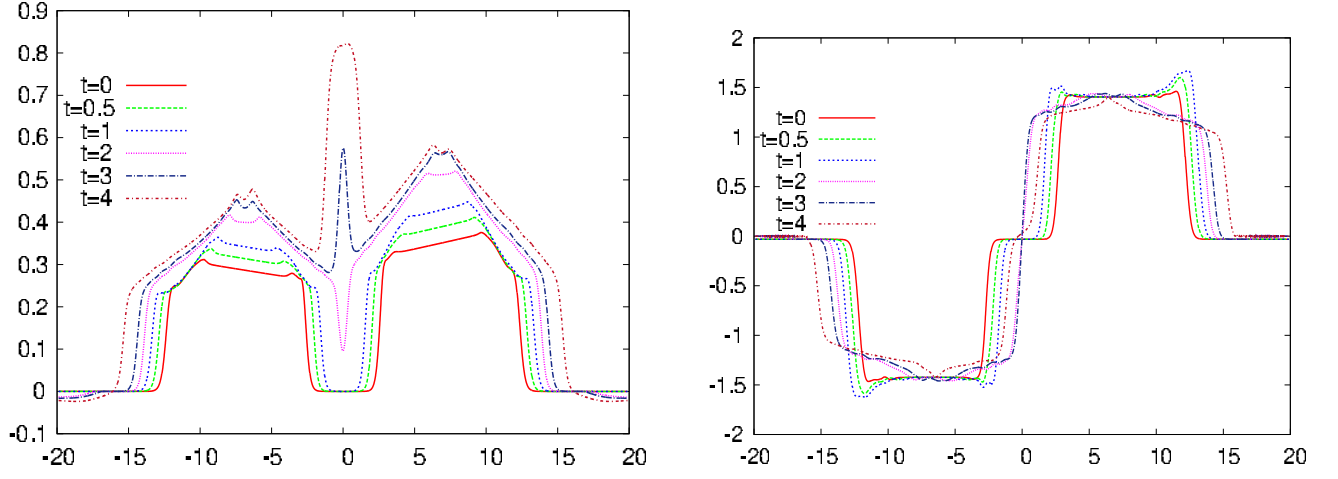


FIG. 14: Snapshots in time leading up to the collision of two bubbles in the collision frame. On the left $A(t, x, y = 0)$ and on the right $\phi(t, x, y = 0)$ where the plane of symmetry is $y = 0$. As the bubbles begin to connect the region between them experiences a greater rate of expansion than either individual bubble. Estimating from the left hand figure we have $\Delta A(x = 0) \simeq 0.5$ during $\delta t = 3 - 2 \simeq 1$, or $H(x = 0) \sim 0.5$. For comparison, $H_1 = 0.05$ and $H_2 = 0.07$ in the nucleation frames and not too different in the collision frame. The right hand picture illustrates that the field which must stretch from ϕ_1 to ϕ_2 does so over a shrinking x coordinate range.

Fig. 15 displays the corresponding surface plot for A and ϕ at $t = 4$. The terms in the metric dependent on A and B grow exponentially. Note that different regions acquire different effective cosmological constants and that the expansion in the region of interaction is much larger than within the unperturbed bubbles.

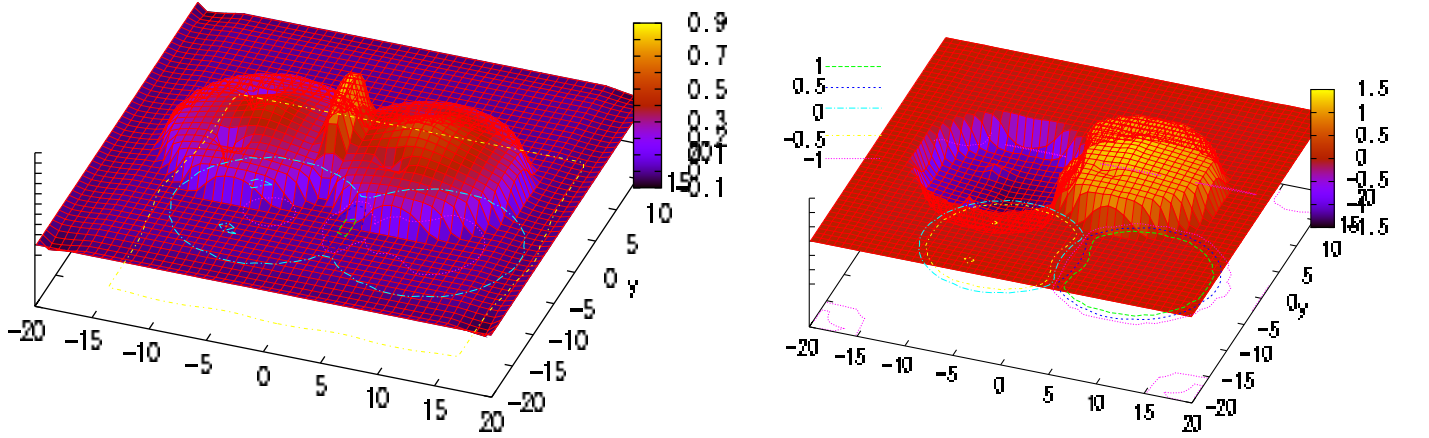


FIG. 15: A surface plot of A (left) and ϕ (right) at $t = 4$ when two bubbles begin to collide. These show the region of the collision. The colored lines below the surface plot are contours for selected values of A and ϕ .

The FLRW equation for maximal symmetry (eq. 3.8 and the approximation $B = 2A$) implies that the conformal Hubble expansion (3.3) depends upon the gradient of scalar field, ϕ_x , its time derivative, ϕ_t and a gradient of the metric, A_x :

$$6H^2(t, x, y) = 4(A_{xx} + A_{yy}) + 2(A_x^2 + A_y^2) + \phi_t^2 + \phi_x^2 + \phi_y^2 + 2e^{2A}V(\phi), \quad (7.1)$$

The dominant contribution on the right hand side may be traced to the large collision induced spatial gradients in the field ϕ . Numerically at $t = 3.0$ we have $\phi_x^2 \sim 8$, $4A_{xx} \sim -3$ and $2A_x^2 \sim \phi_t^2 + 2e^{2A}V \sim 1$ at the origin. They lead to $H \simeq O(1)$. For the assumed geometry the scalar field must connect two different local minima ϕ_1 and ϕ_2 that lie on opposite sides of global minima at ϕ_0 (specifically, $\phi_1 < \phi_0 < \phi_2$) across a distance that shrinks as the two bubble rims approach. Fig. 14 illustrates the phenomenon; see the blue line in the left panel. The gradient in the collision region exceeds that near an isolated bubble wall.

VIII. BUBBLE COLLISION WITHOUT BOOST

We have seen that the bubble speed in the collision frame \dot{R}_{coll} depends upon the boost dx/dt , the velocity of the nucleated bubble center in the collision frame, and \dot{R}_{nuc} , the velocity with which the bubble rim moves in the nucleation frame. If the bubble rim dominates then the distinction between nucleation and collision frames is immaterial. Suppressing the boost makes some physical features more readily apparent. From now on we begin with two bubbles with stationary centers that interact when their rims meet (Figs. 16, 17 and 18).

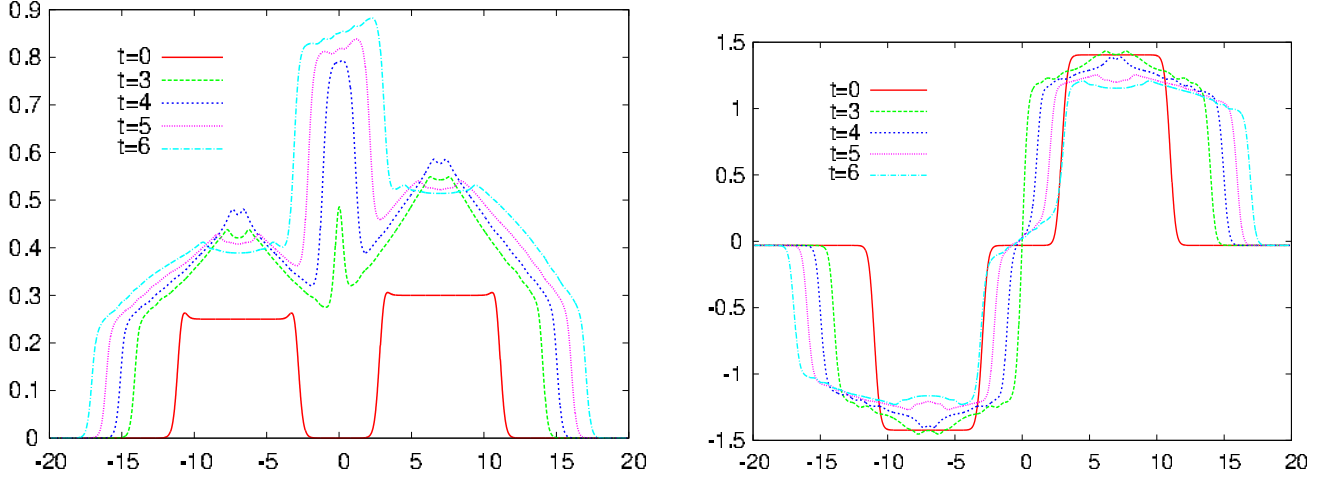


FIG. 16: Snapshots in time of A (left) and ϕ (right) at $y = 0$ for two colliding bubbles. The simulation stops at $t = 6.8$.

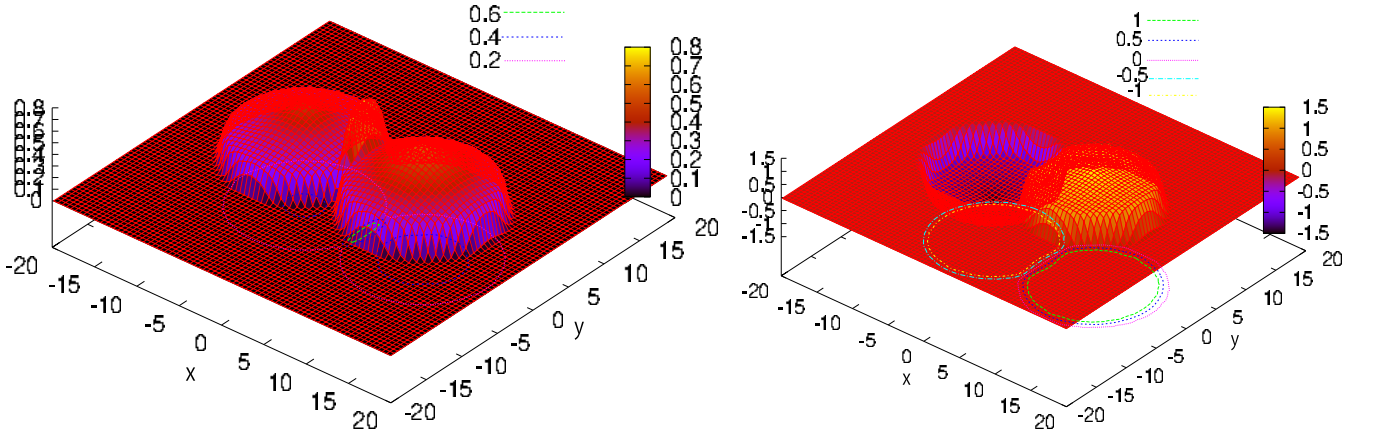


FIG. 17: Surface plot for A (left) and ϕ (right) at $t = 5.5$

The features already identified in the collision frame are clearer in Figs. 16 and 17. The initial bubble rims are identical but the vacua are distinct. The region of interaction experiences a larger rate of expansion than that of either original bubble. The effective Hubble constant during interaction is an order of magnitude larger than that of the individual, non-interacting bubbles. The growth of the metric and the potential in the central region is a multi-step process: the kinetic energy of the bubble walls is localized by the aligned 2+1 collision geometry and focused by increasing spacetime curvature. Part of the field kinetic energy $\phi_t^2/2$ is transformed into potential energy as the field moves away from its global minimum. The field's evolution approaches a classical turning point much like a particle moving towards a rising potential, i.e. the field kinetic energy $\phi_t^2/2 \rightarrow 0$ and the field potential energy V becomes large everywhere except at the field point where $V = 0$. Since spacetime is not homogeneous the turn around does not occur at a single, well-defined point of time. Spatial gradients like ϕ_x^2 are enhanced during the collapse and contribute to the large, effective Hubble constant

Fig. 18 shows the case when the collision involves two bubbles with the *same* false vacuum. The asymmetry apparent in the previous case is suppressed. The kinetic energy of the colliding walls plus the vacuum energy remains. The metric coefficient grows but by a much smaller amount and $H \simeq 0.1$. The symmetry here is important and the gradient term, ϕ_x^2 , is not as large in the aftermath of the collision as it is in the asymmetric case. In the asymmetric collision, it provided the dominant contribution to H .

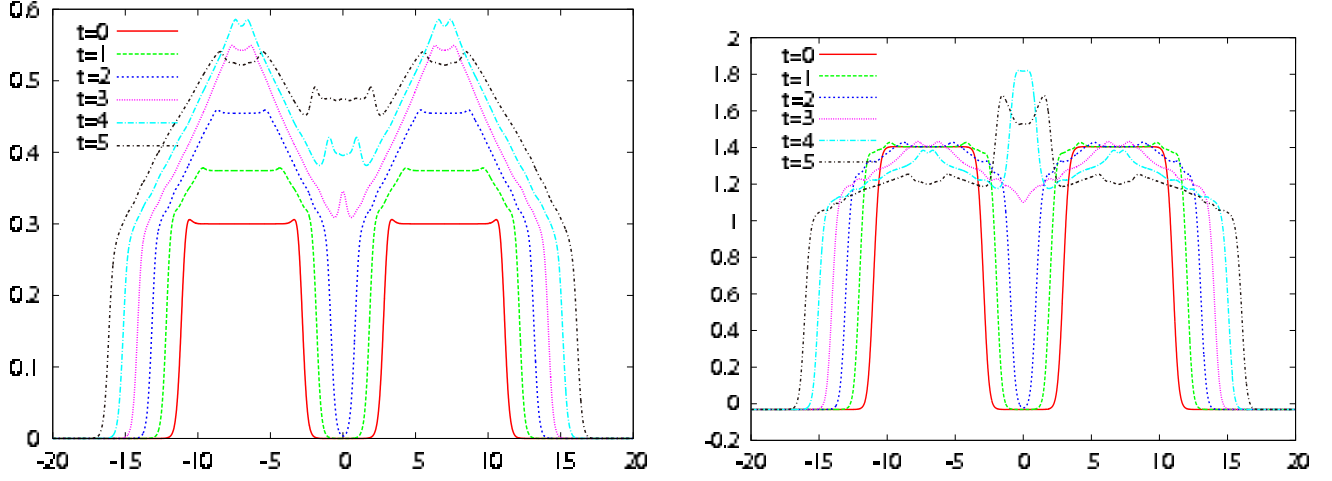


FIG. 18: We plot time evolution of A (left) and ϕ (right) at $y = 0$ until collision of two bubbles. The simulation stops at $t = 5.5$. The scalar field exceeds $\phi = 1$ (where $V(\phi)$ has an unstable equilibrium) throughout most of the collision region. It is unclear which parts will return to the global minimum and which parts to the local metastable minimum.

IX. LONG TIME RESULTS

An important question is the asymptotic outcome of the bubble collision. Which parts of spacetime will remain in metastable local minima and which parts will return to the global minimum? There are two issues which will limit the extent of the runs we can perform and analyze.

As we have previously noted, models for bubbles in 2+1 (cylinder systems) with thin shell junction conditions have been well-studied. For de-Sitter interior, flat exterior the bubble always recollapses in a finite time. Even though our models do not satisfy the thin-wall approximation, the analytic and numerical results for isolated bubbles suggest that all will eventually become singular. The observed growth of the Kretschmann scalar is consistent with this supposition.

When a singularity forms behind an event horizon then one can, in principle, continue to evolve the solution forward in part of spacetime. The hoop conjecture [35] suggests that a horizon forms only when a circular hoop with given size can rotate freely about the object. In the cylinder system no such hoop exists. If a singularity forms at some time it will be a naked singularity and further evolution will be impossible. This situation is seen in sufficiently prolate axisymmetric collapses [36]. Singularity formation in the absence of an apparent horizon is the fundamental limitation to exploring the future evolution of the 2+1 bubble collisions. By contrast, a collision of domain walls in 1+1 formed an apparent horizon that covered and shrouded the singularity [37, 38].

The second issue is more technical. Our method assumes that the deficit angle is small. We see no direct evidence that this assumption is violated. The fact that the constraint equations are poorly satisfied once the Kretschmann scalar curvature begins to diverge is expected. In the future we will examine this issue more directly.

Nonetheless, we can begin to make some interesting observations. The left panel of Fig. 16 shows snapshots of the metric for the collision of two bubbles with different vacua. Initially, A increases at the center of each bubble. At $t \sim 3$ the bubbles begin to overlap and A 's increase slows. Near the center of the bubble we have $A_{tt} \simeq -0.5A_t^2 - 0.25\phi_t^2 + 0.5e^{2AV}$. The fact that $A_{tt} < 0$ (at the center of bubble) follows because the magnitude of A_t and ϕ_t are large. The growth of the metric and the potential in the collapse regions is a multi-step process: we have seen that the aligned 2+1 collision geometry and the development of spacetime curvature focuses energy. Part of the field kinetic energy is transformed into potential energy and enhances V . Since spacetime is not homogeneous the same focusing creates large spatial gradients in ϕ that give rise to large Hubble constants.

The right panel of Fig. 16 show the variation of the field ϕ at the same snapshots. Sections of field with $x > 0$ ($x < 0$) appear to approach the unstable local maxima at $\phi = 1.023$ (-0.97). The field near $x = 0$ is constrained to pass through the global minima of the potential at $\phi = \phi_0$. At $t \sim 4$ only a bit of the field return to the local minima on either side of $x = 0$ (i.e. $\phi = 1.40$ for $x > 0$ and $\phi = -1.42$ for $x < 0$). We cannot be sure if a more violent collision or a different form for $V(\phi)$ might cause more of it to do so. It is apparent that significant parts of the collision region remain close to the unstable local maxima that interpolates between the global and local minima.

Fig. 18 shows analogous results when bubbles having the same vacua collide. Now the field near $x = 0$ is not constrained to pass from positive to negative ϕ . Instead, ϕ is close to the global minimum of the potential at the symmetry point initially. In the collision the field rises, appears to overshoot the local minima $\phi = 1.40$ and then relaxes back to it. The outer regions interpolate between the local minima and local maxima of the potential and this appears to increase in size.

X. IMPLICATIONS

We have explored bubbles in cylindrical symmetry with scalar field stress energy tensors and non-trivial potentials focusing on those with false vacuum inside and flat (nearly Minkowski) space outside. The traditional thin shell description omits the transition region, a part of the spacetime that forms the bridge between de-Sitter interior and Minkowski exterior. The transition region inflates at a lesser rate than the interior of the bubble. In our coordinates the thin shell collapses even while the bridge expands.

Nearby expanding de-Sitter bubbles may collide and create spatially varying vacuum energy density. We evolve examples of colliding systems until a naked singularity forms. At the end of the simulation different local observers measure different vacuum energy densities (effective cosmological constants) in different patches of the universe. Local potential maxima in field space appear to be attractors in the sense that the disturbed fields appear to be poised at or near these maxima. The range in vacuum energy densities is enhanced when different vacua collide. This dynamical mechanism will generally introduce inhomogeneous vacuum energy values, the size of those differences set by the scale between local potential minima/maxima that lie near each other in field space and that are accessible via bubble collisions. It is natural to speculate that the late time appearance of a very small cosmological constant in the universe might be related to this mechanism.

An important caveat for interpreting these results is that spherical bubbles may form horizons whereas cylinder bubbles do not. Part of the interesting dynamics of the cylinder bubble collisions may end up being shielded from outside observers in spherical systems when horizons form. This is an issue that cannot easily be addressed within the context of 2+1 simulations but makes more elaborate 3+1 simulations of great interest.

Acknowledgments

YT would like to thank Masayuki Umemura for discussions on this work. YT also wishes to acknowledge financial supports by a Grant-in-Aid through JSPS Fellow for Research Abroad H26-No.27 and by Research Core for the History of the Universe, University of Tsukuba. This material is based upon work supported by the National Science Foundation under Grant No. 1417132. DC acknowledges NSF's support and the hospitality of Prof. John Barrow, DAMTP and Clare Hall, University of Cambridge. We thank DAMTP, the Centre for Theoretical Cosmology, University of Cambridge, where this work was started.

-
- [1] L. Susskind, In *Universe or multiverse?* ed by B. Carr, pp247-266, hep-th/0302219.
 - [2] J. S. Langer, *Annals Phys.* **54**, 258 (1969).
 - [3] S. R. Coleman, *Phys. Rev. D* **15**, 2929 (1977) Erratum: [*Phys. Rev. D* **16**, 1248 (1977)].
 - [4] S. R. Coleman and F. De Luccia, *Phys. Rev. D* **21**, 3305 (1980).
 - [5] S. W. Hawking and I. G. Moss, *Nucl. Phys. B* **224**, 180 (1983).
 - [6] A. H. Guth and S. H. H. Tye, *Phys. Rev. Lett.* **44**, 631 (1980) Erratum: [*Phys. Rev. Lett.* **44**, 963 (1980)].
 - [7] D. Kazanas, *Astrophys. J.* **241**, L59 (1980).
 - [8] K. Sato, *Phys. Lett.* **99B**, 66 (1981).
 - [9] A. H. Guth, *Phys. Rev. D* **23**, 347 (1981).
 - [10] A. H. Guth and E. J. Weinberg, *Nucl. Phys. B* **212**, 321 (1983).
 - [11] J. Polchinski, hep-th/0603249.
 - [12] K. M. Lee and E. J. Weinberg, *Phys. Rev. D* **36**, 1088 (1987).
 - [13] R. Basu, A. H. Guth and A. Vilenkin, *Phys. Rev. D* **44**, 340 (1991).
 - [14] S. W. Hawking, I. G. Moss and J. M. Stewart, *Phys. Rev. D* **26**, 2681 (1982).
 - [15] R. Easther, J. T. Giblin, Jr, L. Hui and E. A. Lim, *Phys. Rev. D* **80**, 123519 (2009), arXiv:0907.3234.
 - [16] J. T. Giblin, Jr, L. Hui, E. A. Lim and I. S. Yang, *Phys. Rev. D* **82**, 045019 (2010), arXiv:1005.3493.
 - [17] D. i. Hwang, B. H. Lee, W. Lee and D. h. Yeom, *JCAP* **1207**, 003 (2012), arXiv:1201.6109.
 - [18] D. I. Hwang, B. H. Lee, W. Lee and D. H. Yeom, *Nucl. Phys. Proc. Suppl.* **246-247**, 196 (2014).
 - [19] A. Aguirre, M. C. Johnson and A. Shomer, *Phys. Rev. D* **76**, 063509 (2007), arXiv:0704.3473.
 - [20] A. Aguirre and M. C. Johnson, *Rept. Prog. Phys.* **74**, 074901 (2011), arXiv:0908.4105.
 - [21] C. L. Wainwright, M. C. Johnson, H. V. Peiris, A. Aguirre, L. Lehner and S. L. Liebling, *JCAP* **1403**, 030 (2014), arXiv:1312.1357.
 - [22] C. L. Wainwright, M. C. Johnson, A. Aguirre and H. V. Peiris, *JCAP* **1410**, no. 10, 024 (2014), arXiv:1407.2950.
 - [23] M. C. Johnson, C. L. Wainwright, A. Aguirre and H. V. Peiris, *JCAP* **1607**, no. 07, 020 (2016), arXiv:1508.03641.
 - [24] M. Kleban, *Class. Quant. Grav.* **28**, 204008 (2011), arXiv:1107.2593.
 - [25] A. R. Parry, *Anal. Math. Phys.* **4**, no. 4, 333 (2014), arXiv:1210.5269.
 - [26] K. S. Thorne, *Phys. Rev.* **138**, no. 1B, B251 (1965).
 - [27] V. A. Berezin, V. A. Kuzmin and I. I. Tkachev, *Phys. Lett.* **120B**, 91 (1983).
 - [28] K. Maeda, *Gen. Rel. Grav.* **18**, 931 (1986).
 - [29] H. Sato, *Prog. Theor. Phys.* **76**, 1250 (1986).
 - [30] S. K. Blau, E. I. Guendelman and A. H. Guth, *Phys. Rev. D* **35**, 1747 (1987).
 - [31] V. A. Berezin, V. A. Kuzmin and I. I. Tkachev, *Phys. Rev. D* **36**, 2919 (1987).
 - [32] A. Aurilia, M. Palmer and E. Spallucci, *Phys. Rev. D* **40**, 2511 (1989).
 - [33] H. Suzuki, Y. Fujiwara, T. Mishima and A. Hosoya, *Prog. Theor. Phys.* **86**, 411 (1991).
 - [34] K. Sato, H. Kodama, M. Sasaki and K. Maeda, *Phys. Lett. B* **108**, 103 (1982).
 - [35] K. S. Thorne, In *J R Klauder, *Magic Without Magic**, San Francisco 1972, 231-258
 - [36] S. L. Shapiro and S. A. Teukolsky, *Phys. Rev. Lett.* **66**, 994 (1991).
 - [37] Y. i. Takamizu and K. i. Maeda, *Phys. Rev. D* **73**, 103508 (2006).
 - [38] Y. i. Takamizu, H. Kudoh and K. i. Maeda, *Phys. Rev. D* **75**, 061304 (2007), gr-qc/0702138.